Chaos induced breakdown of Bose-Hubbard modeling

Sayak Ray[1], Doron Cohen[2], Amichay Vardi[1]
Department of Chemistry, Ben-Gurion University of the Negev, Beer-Sheva 84105, Israel
Department of Physics, Ben-Gurion University of the Negev, Beer-Sheva 84105, Israel

We show that the Bose-Hubbard approximation fails due to the emergence of chaos, even when excited modes are far detuned and the standard validity condition is satisfied. This is formally identical to the Melnikov-Arnold analysis of the stochastic pump model. Previous numerical observations of Bose-Hubbard breakdown are precisely reproduced by our simple model and can be attributed to many body enhancement of chaos.

The Bose-Hubbard model (BHM) [1, 2] is one of the most prominent tools in the study of interacting many-body systems, no less significant than its celebrated fermionic counterpart [3, 4]. Its use for treating ultracold bosons in shallow optical lattices [5, 6], resulted in landmark experimental demonstrations of the superfluid to Mott insulator quantum phase transition [7–9] and of dynamical quantum phase revivals [10, 11]. These experiments and the subsequent development of quantum engineering techniques provide an unique opportunity to simulate various models and to explore the exotic phases of quantum matter using ultracold atoms [12, 13].

The simplest BHM includes only two modes. Originally introduced in nuclear physics by Lipkin, Meshkov, and Glick [14], two-mode theories apply equally well to Bose-Einstein condensates (BECs) of atoms in the same hyperfine state confined in a double-well trap, and to spinor BECs of atoms with two hyperfine states confined in a single-well trap. Two-mode BHMs are used to describe schemes for squeezing and entanglement [15–17], Josephson oscillations and self-trapping in bosonic Josephson junctions [18–22], the dynamical growth of quantum fluctuations [23–28], and persistent currents and phase slips in superfluid atom circuits [29–34].

The standard validity condition.– Efforts towards realization of quantum simulators assume the validity of the BHM for describing cold atoms in optical lattices. The determination of BHM validity criteria is therefore of utmost importance. The standard criterion [2, 18, 21, 24] is meant to guarantee that the motion be restricted to the lowest Bloch band of the site-chain. As shown below, this condition is given in terms of BHM parameters as,

$$u \ll \frac{\Omega}{K}, \quad u \equiv \frac{NU}{K} \tag{1}$$

where N is the number of particles, U is the on-site interaction, K is the inter-site hopping in the lower band, and Ω is the single particle excitation energy to the next band.

Unexpected breakdown of the BHM.– The BHM was numerically shown to fail in a regime where the standard validity condition holds [35] . This observation was made by comparison of multiconfigurational time-dependent Hartree (MCTDH) simulations of the exact dynamics (including excited modes), with two-mode Bose-Hubbard dynamics. In particular, deviations from the BHM were observed for $u \sim 2$ even for tight traps where Eq.(1) is satisfied. Yet no mechanism was offered to explain this surprising behavior, and a revised validity condition has not been suggested.

Outline.– Here, we show that even if its standard validity condition is satisfied, the BHM is still prone to failure due to the emergence of dynamical chaos. The naive assumption that high lying orbitals that do not participate in the dynamics merely renormalize the hopping elements via virtual transitions does not generally apply. Rather, chaos can be induced via the Melnikov-Arnold mechanism, as in Chirkov's stochastic pump model [37]. Specifically, near-separatrix dynamics becomes stochastic due to the coupling with a high lying orbital. Beyond this zero order resonance, higher order resonances also show up and affect the dynamics. Consequently the lower band becomes entangled with higher bands, as reflected in reduced subsystem entropy measures. Furthermore, we show that the previous numerical observations of BHM breakdown [35] can be attributed to chaos, and are fully reproduced by a simple three mode BHM.

The BHM.– The experimental parameters of a linear 1D chain are the axial trap frequency $\omega_\parallel$, the barrier transmission coefficient T, and the atom number N. The 1D interaction strength is $\lambda_0 = 2\hbar\omega_\perp a_s$, where a_s is the s-wave scattering length, and $\omega_\perp$ is the transverse trap frequency. The atoms mass is m. These parameters define three characteristic length-scales: the axial trap size $L = \sqrt{\hbar/\mathsf{m}\omega_\parallel}$, the healing length $l_c = \sqrt{\hbar/2\mathsf{m}\lambda_0 n}$, and the mean distance between atoms $d = 1/n$, where $n = N/(2L)$ is the average atom density. The standard BHM validity criterion assumes that the interaction energy is too small to bridge the $\Omega = \hbar\omega_\parallel$ gap between the lowest Bloch band and the first excited band. In terms of characteristic lengths, BHM is supposed to apply when $l_c \gg L$, i.e. when the healing length is larger than the single-site trap size. This can be written as $\nu \ll 1$, where $\nu \equiv (L/l_c)^2 = \lambda_0 n/(\hbar\omega_\parallel)$. The M-site chain is then described by the tight-binding Hamiltonian,

$$\hat{H}_{\rm BH} = \frac{U}{2}\sum_{i=1}^{M}\hat{n}_i(\hat{n}_i - 1) - \frac{K}{2}\sum_{\langle ij\rangle}^{M}(\hat{a}_i^\dagger\hat{a}_j + \hat{a}_j^\dagger\hat{a}_i) \tag{2}$$

where $\hat{a}_i$ and $\hat{n}_i$ are the bosonic annihilation and number

operators, $\langle ij\rangle$ denotes summation over nearest neighbors, and the effective parameters are the tunnel-splitting $K \approx \hbar\omega\sqrt{T}$, and the interaction-strength $UN \approx \lambda_0 n$. The small parameter ν can hence be expressed in terms of BHM parameters, as $\nu = NU/\Omega$, and the standard BHM validity criterion $\nu \ll 1$ takes the form of Eq.(1).

In order to investigate the chaos-induced breakdown of the BHM, we consider the $M = 2$ (dimer) case, and emulate the effect of excited Bloch bands by adding to Eq.(2) a single detuned bosonic mode:

$$\hat{\mathcal{H}} = \hat{H}_{\rm BH} + \Omega\hat{n}_0 + \frac{U}{2}\hat{n}_0(\hat{n}_0-1) - \frac{\kappa}{2}\sum_{i=1}^{2}(\hat{a}_i^\dagger\hat{a}_0 + \text{h.c.}) \quad (3)$$

where Ω and κ are respectively, the detuning and coupling of the auxiliary bosonic mode '0'. In our calculation we set $\hbar = 1$ and determine the units of time such that the hopping frequency is $K = 1$.

Dynamics.– The motional constants of the Hamiltonian (3) are the three-mode energy E and the total three-mode particle number N. In what follows, we refer to the full many-body dynamics, obtained from popagation with the Hamiltonian (3) as *quantum* motion, whereas its large N classical limit, that amounts to replacing the field operators $\hat{a}_i$ by c-numbers $a_i = \sqrt{n_i}\exp(i\phi_i)$, is denoted as *classical* motion. Using N conservation to eliminate the overall phase, the classical canonical variables are the dimer's population imbalance $n = n_1 - n_2$, the relative phase $\phi = \phi_1 - \phi_2$, and the auxiliary mode's population n_0 and phase ϕ_0. For further detail on the dynamical equations, see supplementary material [39].

Semiclassical perspective.– In Fig.1(a), we plot the pendulum-like classical phase space of the dimer [20, 21, 28], where $\kappa = 0$. Since the isolated dimer has just one degree of freedom, its motion is necessarily integrable. The dimensionless interaction parameter u distinguishes between three *interaction regimes* [2, 21, 28]: Rabi (u<1); Josephson (1<u<N^2); and Fock (u>N^2). Within the Josephson interaction regime, the phase-space consists of a low energy Rabi-Josephson oscillation region [18, 22] and a high-energy self-trapping region [19–21], that are separated by a mid-energy separatrix [28].

In panels 1(b)-(f), we set the coupling to $\kappa = 0.5$ and study the effect of the third mode for various values of its detuning Ω. It should be noticed that different trajectories do not have the same energy E, hence they do not belong to the same Poincare section. One observes that the addition of a third mode opens the way to non-integrable motion resulting in stochastic regions in phase space due to non-linear resonances.

Consider first the low Ω panels 1(b)-(c). In this regime Eq.(1) is not satisfied, and the trajectories are strongly affected by the coupling to the excited mode. Not only the separatrix motion is affected: in panel (b) most Rabi-Josephson trajectories become chaotic; while in panel (c) chaotic motion is obtained mainly for self-trapped trajectories.

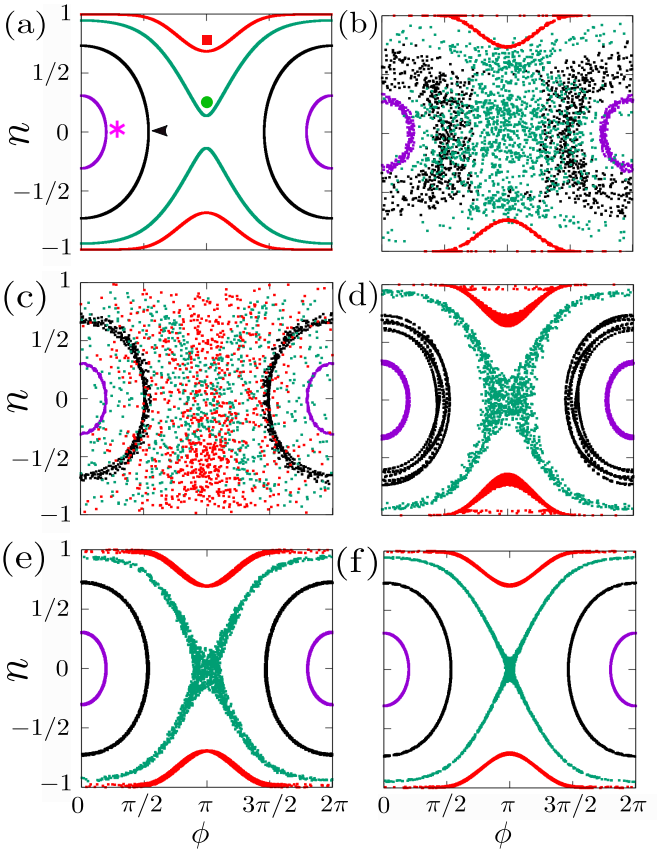

FIG. 1. (Color online) Phase-space illustration of Bose-Hubbard dynamics. Panel (a) is for an isolated two modes system. It shows representative Rabi-Josephson (magenta-star, black-arrow), near-separatrix (green-circle), and self-trapped (red-square) trajectories for $u = 3$ and $\kappa = 0$. Panels (a-f) are for a two-mode system coupled to a third detuned mode ($\kappa = 0.5$), with $\Omega = 0.5, 2.0, 4.5, 6, 7$, respectively. They show $\phi_0 = 0$ Poincare sections for the same initial conditions as in (a), while the third orbital is initially empty ($n_0 = 0$).

By contrast, for the large Ω panels 1(d)-(f), the validity criterion of Eq.(1) is satisfied, and one expects the far-detuned mode to have a negligible effect. Indeed, this seems to be the case in most regions of phase space. However, a stochastic strip remains in the vicinity of the separatrix, even when the detuning is large. This is expected from the standard theory of non-linear resonances, and can be quantified as in the Melnikov-Arnold analysis of the stochastic pump model [37]. Thus, due to chaos, the BHM breaks down for near-separatrix motion, and in the vicinity of resonances, even when the standard validity condition is fully met.

Deviation measure.– To quantify the deviation from the two-mode BHM, we consider the instantaneous difference between the population imbalance $n(t)$ obtained by including the extra mode, and the same quan-

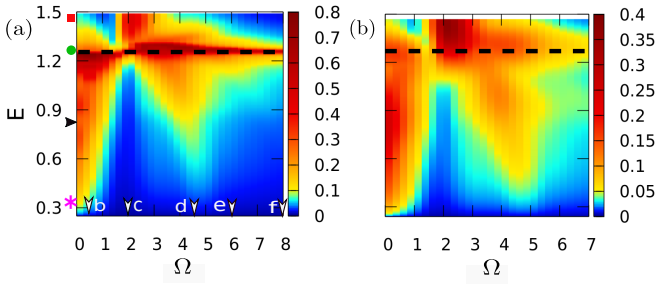

FIG. 2. (Color online) The deviation d of Eq. (4), plotted as a function of the trajectory's energy E and the detuning Ω: (a) classical simulations; (b) quantum simulations with $N = 100$, launched at the corresponding coherent state. The parameters $u = 3$ and $\kappa = 0.5$ are the same as in Fig. 1. Dashed line marks the separatrix energy. The detuning values of Fig. 1(b)-(f) are marked on the horizontal axis, and the energies of the plotted trajectories are marked on the vertical axis with the same marker-convention.

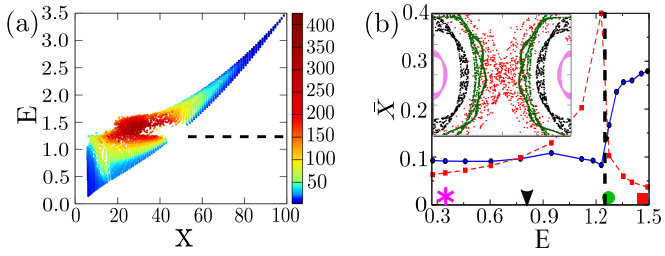

FIG. 3. (color online) (a) The spectrum $\{E_\nu\}$ for $N = 100$, $u = 3$, $\kappa = 0.5$, $\Omega = 2$. Each point is positioned horizontally according to $X_\nu = \langle \hat{n}_0 \rangle$, and color coded by participation number M_ν. Strong mixing is witnessed at the separatrix energy (dashed line) and extends to the region above it. (b) Time averaged occupation of the third mode, $\bar{X} \equiv \overline{n_0(t)}$, obtained from three-mode classical dynamics (solid blue) as a function of E, compared with the estimate $\bar{X} \sim \kappa^2/\omega^2(E)$ (red dashed) that assumes quasi-integrable orbits. The separatrix energy is indicated by vertical dashed line, while the energies of the trajectories in Fig.1 are indicated by symbols. The inset shows the stroboscopic map for the two mode BHM in the presence of driving with frequency $\Omega = 2$ and intensity $A = \sqrt{\bar{X}}$. It corresponds to Fig.1c and has same axes.

tity $n_{\rm BH}(t)$ obtained in the two-mode BHM approximation, averaged over $T = 2\pi$,

$$d(E, \Omega) = \frac{1}{T} \int_0^T |n(t) - n_{\rm BH}(t)| dt \qquad (4)$$

In Fig.2(a) we plot d as function of the trajectory's energy E and the detuning Ω. Since all simulations are launched with $n_0(0) = 0$, the total energy E equals the initial dimer energy. The trajectories that are sampled in panels (b-f) of Fig.1 are indicated. One observes that the deviation d is large for trajectories in regions of stochastic motion. The corresponding quantum results are displayed in Fig.2(b). Initial conditions in these quantum simulations were three-mode coherent states,

$$|n, \phi, n_0, \phi_0\rangle = \frac{1}{\sqrt{N!}} \left(\sum_{i=0}^{2} \alpha_i \hat{a}_i^\dagger \right)^N |{\rm Vac}\rangle \ , \qquad (5)$$

where $\alpha_1 = \sqrt{(N+n)}/2$ and $\alpha_2 = \sqrt{(N-n)/2} e^{i\phi}$ are the same as in the classical simulations and $\alpha_0 = \sqrt{n_0} e^{i\phi_0}$ is set to zero. We observe good quantum-classical agreement, with some blurring of classical features due to the finite uncertainty width of the initial coherent state.

Many body enhancement of chaos.– The emergence of stochastic regions in Fig. 1 and the deviation depicted in Fig. 2 would have been obtained also if the two-mode system is driven at frequency Ω. However, as shown below, the many-body aspect of incorporating an auxiliary mode in the Hamiltonian, amounts to considerable enhancement of chaos with respect to the corresponding driven system.

Consider the representative quantum spectrum in Fig. 3(a). Each point represents an exact eigenstate ν of the Hamiltonian in Eq. (3), positioned horizontally according to $X_\nu = \langle \nu | \hat{n}_0 | \nu \rangle$, vertically according to its energy E_ν, and color coded by its participation number $M_\nu = \left(\sum_m |\langle m|\nu\rangle|^4 \right)^{-1}$, where m labels the unperturbed eigenstates of the uncoupled ($\kappa = 0$) system. Large M_ν implies that many eigenstates are mixed due to the $\kappa \neq 0$ coupling.

The Floquet states of any driving scenario would only mix $|m\rangle$ states with the same n_0, i.e. driving corresponds to *vertical* mixing in Fig.3(a). By contrast, referring to the (X, E) diagram of the three-mode spectrum, we see that chaos in the vertical direction induces mixing also in the horizontal direction. Thus, the possibility of back action by the two mode dynamics on the auxiliary mode, results in enhanced chaos.

Considering the form of the two-mode dynamical equations $\dot{a}_j = ... + i(\kappa/2)a_0$ [39], the corresponding c-number driving would be obtained by substituting $a_0 = \sqrt{A} \exp(-i\Omega t)$, where A is a free constant parameter. To reproduce the effect of the third mode, the effective drive intensity A should reflect its occupation n_0. Since from inspection of Fig.3(a) it is clear that this occupation is larger in regions of chaos due to the many body mixing, the third mode's effect corresponds to an amplified drive intensity in these regions, i.e. to *many body enhancement of chaos*. This observation is somewhat reminiscenct of the *dynamical enhancement of small perturbations* in the nuclear physics context [38].

We may attempt to evaluate the effective A from the time averaged occupation in the 3rd orbital $\bar{X} = \overline{n_0(t)}$. If chaos was not present, we could estimate $\bar{X}$ from the equation of motion $\dot{a}_0 \approx i(\kappa/2)(a_1 + a_2)$ leading to $\bar{X} \sim \kappa^2/\omega^2(E)$, where $\omega(E)$ is the frequency of the unperturbed dimer oscillations. The comparison of this estimate with the actual three-mode result in Fig.3(b),

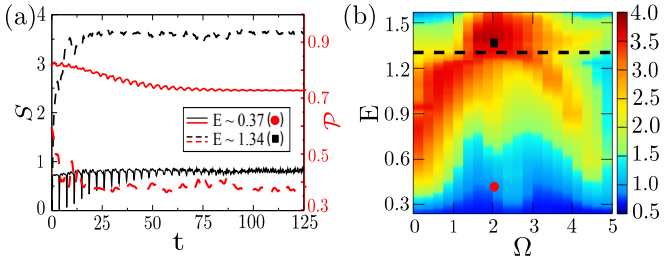

FIG. 4. (color online) (a) Time evolution of the entanglement entropy S and the single-particle purity $\mathcal{P}$ for a chaotic (dashed) and for a quasi-integrable (solid) three-mode dynamics, starting from an eigenstates of the unperturbed two-mode system. (b) The time-averaged entanglement entropy $\overline{S(t)}$ as a function of E and Ω. Markers indicate the parameter values for the curves in (a). The other parameters are as in Fig. 2.

demonstrates the enhancement of $\bar{X}$ in chaotic regions. The inset in Fig.3(b) shows the dynamics of a driving scenario where $A = \bar{X}$ is the numerically extracted actual value of $\bar{X}$. Comparing with Fig.1c we realize that even this procedure still underestimates the enhanced chaos.

One-particle purity.– In Fig.4a we prepare the system in representative eigenstates $|m\rangle$, with vacant 3rd orbital ($n_0 = 0$), of the unperturbed ($\kappa = 0$) Hamiltonian (3), and plot the time dependence of the one-particle purity $\mathcal{P} = \mathrm{Tr}\left(\rho_{sp}^2\right)$, where $\rho_{sp} = \langle \hat{a}_i^\dagger \hat{a}_j \rangle$ is the reduced single particle density matrix. The one-particle purity value lies in the range $1/3 < \mathcal{P} < 1$ and its inverse indicates the number of modes required to capture the dynamics. Thus $\mathcal{P} \approx 1$ indicates the validity of mean-field theory, wherein all particles occupy a single orbital, $1/2 < \mathcal{P} < 1$ indicates two-orbital dynamics (strictly speaking, this range will also be obtained if the pertinent two orbitals project onto the auxiliary mode), while $\mathcal{P} < 1/2$ clearly indicates the breakdown of the two-mode approximation. The latter is observed if the dynamics is affected by chaos.

Generation of entanglement.– The addition of an excited mode also implies that *entanglement* could be generated between the dimer modes and the high frequency mode. The entanglement entropy is defined as $S = \mathrm{Tr}(\rho_\mathrm{d} \ln \rho_\mathrm{d}) = \mathrm{Tr}(\rho_0 \ln \rho_0)$, where $\rho_\mathrm{d} = \mathrm{Tr}_0(\rho)$ and $\rho_0 = \mathrm{Tr}_\mathrm{d}(\rho)$ are the many-body reduced density matrices of the dimer and the auxiliary mode, respectively. In Fig.4(a) we plot the time evolution of S for a couple of representative simulations. Carrying out such simulations at various values of Ω, for all dimer eigenstate preparations (distinguished by E) we plot the time-averaged $\overline{S(t)}$ in Fig.4(b). We observe that the entanglement entropy is large in region that support chaotic motion. Comparing with Fig.2 we see that chaos dominates at the vicinity of the separtrix: just below it for $\Omega < 1.5$, and just above it for $\Omega > 1.5$. Corresponding red regions below and above the separatrix energy in Fig.4(b) show the entanglement fingerprint of chaos.

Reconstruction of BHM breakdown.– In Fig.5(a)

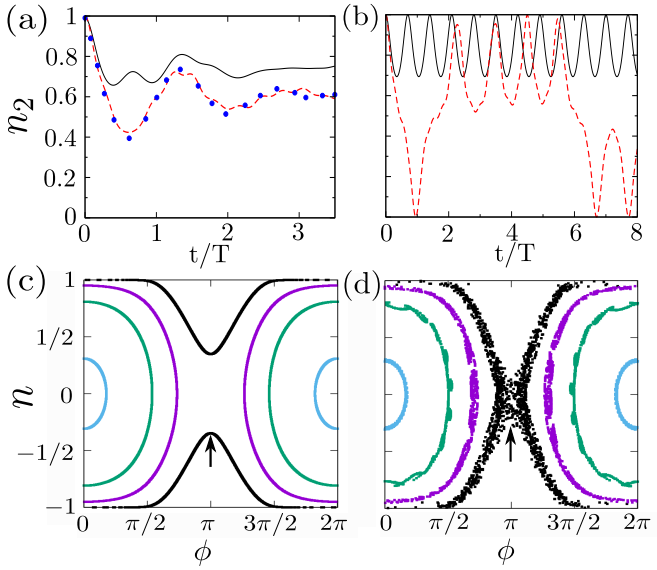

FIG. 5. (Color online) Comparison with Ref. [35]: (a) Population dynamics obtained by the two mode BHM (solid black), the MCTDH method (Blue circles), and our simple model (dashed red). The data points for the MCTDH dynamics are extracted from Fig. 1d in Ref. [35]; (b) The corresponding classical dynamics; (c) The phase space structure of the isolated two-mode BHM ($\kappa = 0$); (d) The corresponding Poincare sections at $\phi_0 = 0$ in the presence of the excited mode with detuning $\Omega = 5$ and coupling $\kappa = 0.75$.

we compare representative MCTDH population dynamics results from Ref. [35] with the results of our simple $2+1$ modes model, for the same parameters and initial conditions. The excellent agreement between the two methods, confirms that the source of BHM breakdown in [35] is indeed the emergence of near-separatrix chaos in the effectively three-orbital classical motion, as illustrated in Fig.5(b)-(d). In fact, as shown in the supplementary material [39] we were able to reproduce *all* the results of Ref. [35] using our model, including the thermalization of a self-trapped trajectory for large values of u where the validity condition (1) is violated and the two mode approximation breaks down. This thermalization too, is the result of chaotic ergodization of the type shown in Fig.1(c).

Discussion.– The description of optical lattices in state-of-the-art quantum simulations, by the BHM should not be taken for granted. It is distinct from the truncation of a high-lying band of states in electronic systems that features a spectral gap. Even few-particle systems impose severe limitations [36], while in this work we have considered a many-body system ($N \gg 1$) with no gap (Fig.3a). Using a semiclassical perspective, we have shown that the emergence of chaos requires one to forego the naive reasoning. The effect is amplified due to the many-body mixing of the eigenstates, and provides new insight for the relevance of the formal MCTDH method.

Acknowledgements.– This research was supported by the Israel Science Foundation (Grant No. 283/18)

[1] M. P. A. Fisher, P. B. Weichman, G. Grinstein, and D. S. Fisher, Phys. Rev. B **40**, 546 (1989).
[2] A.J. Leggett, Rev. Mod. Phys. **73**, 307 (2001).
[3] Proc. R. Soc. Lond. Ser. A Math. Phys. Eng. Sci., **276**, 238 (1963).
[4] M.C. Gutzwiller Phys. Rev. Lett. **10**, 159 (1963).
[5] I. Bloch, Nat. Phys. **1**, 23 (2005).
[6] K. V. Krutitsky, Phys. Rep. **607**, 1 (2016).
[7] D. Jaksch, C. Bruder, J. I. Cirac, C. W. Gardiner, P. Zoller, Phys. Rev. Lett. **81**, 3108 (1998).
[8] C. Orzel, A. K. Tuchman, M. L. Fenselau, M. Yasuda, M. A. Kasevich, Science **291**, 2386 (2001).
[9] M. Greiner, O. Mandel, T. Esslinger, T. W. Hänsch, I. Bloch, Nature **415**, 39 (2002).
[10] M. Greiner, O. Mandel, T. W. Hänsch, I. Bloch, Nature **419**, 51 (2002).
[11] S. Will, T. Best, U. Schneider, L. Hackermüller, D. S. R. Lühmann, and I. Bloch, Nature **465**, 197 (2010).
[12] M. Lewenstein, A. Sanpera, V. Ahufinger, B. Damski, A. Sen(De), and U. Sen, Adv. Phys., **56**, 243 (2007).
[13] I. Bloch, J. Dalibard, and S. Nascimbene, Nat. Phys. **8**, 267 (2012).
[14] H. J. Lipkin, N. Meshkov, and A. J. Glick, Nucl. Phys. **62**, 188 (1965); N. Meshkov, A. J. Glick, and H. J. Lipkin, Nucl. Phys. **62**, 199 (1965); A. J. Glick, H. J. Lipkin, and N. Meshkov, Nucl. Phys. **62**, 211 (1965).
[15] G.-B. Jo, Y. Shin, S. Will, T. A. Pasquini, M. Saba, W. Ketterle, D. E. Pritchard, M. Vengalattore and M. Prentiss, Phys. Rev. Lett. **98**, 030407 (2007).
[16] J. Esteve, C. Gross, A. Weller, S. Giovanazzi, and M. K. Oberthaler, Nature **455**, 1216 (2008).
[17] M. F. Riedel, P.l Böhi, Yun Li, T. W. Hänsch, A. Sinatra, and P. Treutlein Nature **464**, 1170 (2010).
[18] G. J. Milburn, J. Corney, E. M. Wright, and D. F. Walls Phys. Rev. A **55**, 4318 (1997).
[19] A. Smerzi, S. Fantoni, S. Giovanazzi, and S. R. Shenoy, Phys. Rev. Lett. **79**, 4950 (1997).
[20] M. Albiez, R. Gati, J. Fölling, S. Hunsmann, M. Cristiani, and M. K. Oberthaler Phys. Rev. Lett. **95**, 010402 (2005).
[21] R. Gati, M.K. Oberthaler, J. Phys. B **40**, 61(R) (2007).
[22] S. Levy, E. Lahoud, I. Shomroni, and J. Steinhauer, Nature **449**, 579 (2007).
[23] A. Vardi and J. R. Anglin, Phys. Rev. Lett. **86**, 568 (2001).
[24] J. R. Anglin and A. Vardi, Phys. Rev. A **64**, 013605 (2001).
[25] Y. Khodorkovsky, G. Kurizki, and A. Vardi, Phys. Rev. Lett. **100**, 220403 (2008).
[26] E. Boukobza, M. Chuchem, D. Cohen and A. Vardi, Phys. Rev. Lett. **102**, 180403 (2009).
[27] E. Boukobza, M. G. Moore, D. Cohen, and A. Vardi, Phys. Rev. Lett. **104**, 240402 (2010).
[28] M. Chuchem, K. Smith-Mannschott, M. Hiller, T. Kottos, A. Vardi, and D. Cohen, Phys. Rev. A, 82, 053617 (2010).
[29] K. C. Wright, R. B. Blakestad, C. J. Lobb, W. D. Phillips, and G. K. Campbell, Phys. Rev. Lett. **110**, 025302 (2013).
[30] S. Eckel, J. G. Lee, F. Jendrzejewski, N. Murray, C. W. Clark, C. J. Lobb, W. D. Phillips, M. Edwards, and G. K. Campbell, Nature **506**, 200 (2014).
[31] O. Fialko, M.-C. Delattre, J. Brand, and A. R. Kolovsky, Phys. Rev. Lett. **108**, 250402 (2012).
[32] G. Arwas and D. Cohen,, New J. Phys. **18**, 015007 (2016).
[33] G. Arwas and D. Cohen, Phys. Rev. B **95**, 054505 (2017).
[34] Geva Arwas, Doron Cohen, Frank Hekking, and Anna Minguzzi, Phys. Rev. A **96**, 063616 (2017).
[35] K. Sakmann, A. I. Streltsov, O. E. Alon and L. S. Cederbaum, Phys. Rev. Lett. **103**, 220601 (2009).
[36] J. Dobrzyniecki and T. Sowiski, Eur. Phys. J. D **70**, 83 (2016).
[37] Boris. V. Chirikov, Phys. Rep. **52**, 263 (1979).
[38] V. V. Flambaum, Phys. Scr. **1993**, 198 (1993).
[39] See supplementary material.

SUPPLEMENTARY MATERIAL

DYNAMICAL EQUATIONS

To study the dynamics governed by the Hamiltonian of Eq. (3), we first write down the Heisenberg equations of motion $i\dot{\hat{a}}_i = [\hat{a}_i, \hat{\mathcal{H}}]$, for the bosonic annihilation operators $\hat{a}_i$:

$$i\dot{\hat{a}}_1 = -\frac{1}{2}\hat{a}_2 + \frac{U}{2}(\hat{n}_1\hat{a}_1 + \hat{a}_1\hat{n}_1) - \frac{\kappa}{2}\hat{a}_0 \ , \tag{6a}$$

$$i\dot{\hat{a}}_2 = -\frac{1}{2}\hat{a}_1 + \frac{U}{2}(\hat{n}_2\hat{a}_2 + \hat{a}_2\hat{n}_2) - \frac{\kappa}{2}\hat{a}_0 \ , \tag{6b}$$

$$i\dot{\hat{a}}_0 = \Omega\hat{a}_0 - \frac{\kappa}{2}(\hat{a}_1 + \hat{a}_2) + \frac{U}{2}(\hat{n}_0\hat{a}_0 + \hat{a}_0\hat{n}_0) \ . \tag{6c}$$

Two conserved quantities constrain the dynamics: One is the total energy and the other is the total number of particle resulting from $[\hat{\mathcal{H}}, \hat{N}] = 0$ where, $\hat{N} = \sum_{i=0}^{2} \hat{n}_i$.

Classical dynamics: In the large N-limit the field operators can be replaced by c-numbers such as, $\hat{a}_i \to a_i$, $\hat{n}_i \to n_i$, where, $a_i = \sqrt{n_i}e^{i\phi_i}$, $n_i = |\alpha_i|^2$. The classical populations and phases $\{n_i, \phi_i\}$ serve as conjugate dynamical variables. The equation of motion for the complex variables a_i are thus given by,

$$i\dot{a}_1 = -\frac{1}{2}a_2 + u|a_1|^2a_1 - \frac{\kappa}{2}a_0 \ , \tag{7a}$$

$$i\dot{a}_2 = -\frac{1}{2}a_1 + u|a_2|^2a_2 - \frac{\kappa}{2}a_0 \ , \tag{7b}$$

$$i\dot{a}_0 = \Omega a_0 - \frac{\kappa}{2}(a_1 + a_2) + u|a_0|^2a_0 \ , \tag{7c}$$

where, $u = UN/K$. Using N conservation, we eliminate one degree of freedom, leaving $n = n_1 - n_2$, $\phi = \phi_1 - \phi_2$, n_0, and ϕ_0 as the dynamical variables of our two-freedoms system. Evolving Eqs. (7), we obtain the classical results of Fig. 1.

Quantum dynamics: The quantum Fock states of the three-mode models are $|n, n_0\rangle$ where, $n_0 \in [0, N]$ and $n \in [-(N - n_b), (N - n_b)]$. The operation of the field operators is e.g. $\hat{a}_1^\dagger\hat{a}_2\,|n, n_0\rangle = \sqrt{n_2(n_1 + 1)}\,|n + 2, n_0\rangle$ where, $n_1 = (N - n_b + n)/2$ and $n_2 = (N - n_b - n)/2$. Given some initial quantum preparation $|\Psi(0)\rangle$, we employ the Fock state representation to obtain the time evolved state $|\Psi(t)\rangle = e^{-i\hat{\mathcal{H}}t}|\Psi(0)\rangle$.

COMPARISON WITH PREVIOUS NUMERICAL RESULTS

In Ref. [35], deviations from the two-mode BHM are observed numerically, by employing the multiconfigurational time-dependent Hartree (MCTDH) method, to obtain exact double-well dynamics that include the effect of excited modes. The dynamics shown in Fig. 1 of [35], that is reproduced here in Fig. S1, demonstrate that the BHM breaks down even when u is small with respect to Ω/K and Eq. (1) is satisfied. The initial preparation with $n_2 = N$ gives Rabi-Josephson oscillations for $u < 2$ or self-trapped motion for $u > 2$. For $u \approx 2$ it lies near the separatrix. Thus, Panels (a) and (b) illustrate the validity of the BHM for Rabi-Josephson oscillations, but panels (c) and (d) show its failure to depict near-separatrix motion.

The dashed red lines in Fig.S1 corresponds to quantum propagation using the Hamiltonian of Eq. (3). Our simple model clearly reproduces the results of the MCTDH model (blue circles) to great accuracy. We therefore deduce that the numerical observations in Ref. [35] can be attributed in essence, to our mechanism of BHM failure due to chaos.

The obsevred agreement extends beyond the weak-interaction regime where the BHM validity condition is satisfied. In Fig. 2 of Ref. [35], the interaction strength is large enough to violate Eq. (1). Thus, while the $n_2 = N$ preparation is deep in the self trapped region in this case, so that almost no population oscillation exists in its two-mode dynamics, the excited mode can affect the entire phase-space, and in particular can transform self-trapped trajectories to chaotic ones, as in Fig.1(c). The result is the thermalization of the population distribution that was noted in [35]. In Fig.S2 we reproduce this result for the pertinent parameters, showing that it too is attributed to chaos.

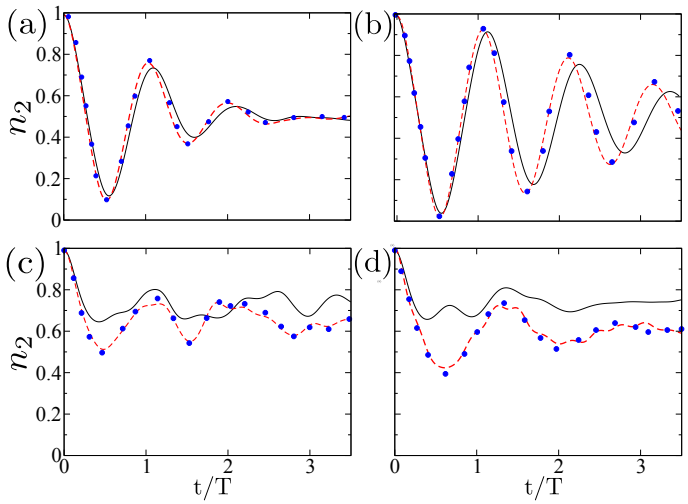

FIG. S1. (Color online) Breakdown of the BHM despite weak interaction: Comparison of population dynamics obtained using the two-mode BHM (solid black line), the MCTDH method of Ref. [35] (blue circles), and our $2+1$ mode model Eq. (3). The parameters and the initial preparation with $n_2 = N$ are identical to Fig. 1 of Ref. [35]: (a) $u = 1.4$, $N = 20$; (b) $u = 1.35$, $N = 100$; (c) $u = 2.26$, $N = 20$; (d) $u = 2.17$, $N = 100$. The parameters used in our model are $\Omega = 5$ in all panels, $\kappa = 0.65$ in a,b and 0.75 in c,d.

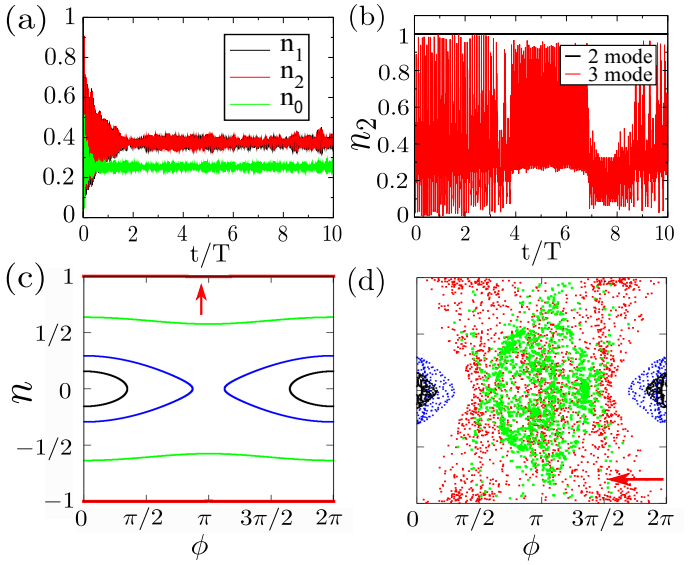

FIG. S2. (Color online) Chaotic ergodization at strong interaction: (a) Quantum population dynamics obtained by time propagation with the Hamiltonian of Eq. (3) with $\Omega = 30$ and $\kappa = 40$, for the same parameters as in Fig. 2 of Ref. [35]: $u = 43.4$, $N = 100$; (b) Classical population dynamics for the same parameters using either the two-mode BHM (black line, depicting a nearly-stationary point at $n_2 = N$) or the Hamiltonian of Eq. (3) (red line, exploring the entire allowed population range); (c) The two-mode phase-space; (d) Poincare sections in the $2+1$ mode phase space, as in Fig.1. The self-trapped dimer at $n_2 = N$ becomes chaotic due to the coupling to the auxiliary mode and explores the entire stochastic band, resulting in the 'thermalization' of the population distribution.